LETTER

doi:10.1038/nature14153

Grid cell symmetry is shaped by environmental geometry

Julija Krupic[1]*, Marius Bauza[1]*, Stephen Burton[1], Caswell Barry[1] & John O'Keefe[1,2]

Grid cells represent an animal's location by firing in multiple fields arranged in a striking hexagonal array[1]. Such an impressive and constant regularity prompted suggestions that grid cells represent a universal and environmental-invariant metric for navigation[1,2]. Originally the properties of grid patterns were believed to be independent of the shape of the environment and this notion has dominated almost all theoretical grid cell models[3–6]. However, several studies indicate that environmental boundaries influence grid firing[7–10], though the strength, nature and longevity of this effect is unclear. Here we show that grid orientation, scale, symmetry and homogeneity are strongly and permanently affected by environmental geometry. We found that grid patterns orient to the walls of polarized enclosures such as squares, but not circles. Furthermore, the hexagonal grid symmetry is permanently broken in highly polarized environments such as trapezoids, the pattern being more elliptical and less homogeneous. Our results provide compelling evidence for the idea that environmental boundaries compete with the internal organization of the grid cell system to drive grid firing. Notably, grid cell activity is more local than previously thought and as a consequence cannot provide a universal spatial metric in all environments.

Navigation is performed on the basis of information about self-motion and external cues, including enclosure geometry, the latter dominating non-geometric information such as visual landmarks, textures and smells[11–13]. In mammals the hippocampal formation is required for spatial navigation[14] and its neurons encode the animal's position (place cells[15] and grid cells[1]), head direction (head direction cells[16]) and proximity to boundaries (boundary cells[17,18]). The spatial activity of boundary and place cells is known to be affected by environmental geometry[17–19]. Grid cells may also be influenced by changes to boundaries, in particular reflecting distortions of a familiar enclosure by rescaling in the same direction[7]. These changes ameliorate with time and cells tend to return towards their canonical patterns, reinforcing the idea that internal processes at the individual cell or network level predominantly determine the grid pattern[2]. Here we demonstrate that environmental geometry exerts an important and permanent influence on grid cell firing. Under certain circumstances, it can overcome internal network processes and lead to profound distortions of the grid pattern.

In geometrically symmetrical enclosures such as circles, distal cues control the orientation of grid patterns which follow cue rotation[1]. In contrast, we found that in geometrically polarized enclosures, such as squares, greater control is exercised by the arena. A 45° rotation of the arena commensurately rotates the grid pattern despite prominent distal cues remaining stationary (Fig. 1a, b, mean grid rotation ± 42.5° ± 2.9° (mean + s.e.m., here and elsewhere), $n = 5$ rats/5 modules, 19 grid cells, not different from 45°, $P = 0.44$, $t = -0.85$, $n = 5$, df = 4, one-sample t-test). Notably, no changes were observed for 90° rotations for which geometry remains unchanged but local cues such as smells and textures move (mean grid orientation 1.1° ± 0.9° not different from 0°, $P = 0.29$, $t = 1.21$, $n = 5$, df = 4, one-sample t-test).

We explored which aspects of the grid pattern were affected by environmental geometry, beginning with the influence of the enclosure walls over grid orientation. A total of 275 grid cells (62 modules, 41 rats) were recorded while animals foraged in square enclosures (Fig. 1c and Extended Data Figs 1 and 2). Across rats, the orientation of the grids aligned at a mean angle of 8.8° ± 0.6° to the enclosure walls (Fig. 1d, e; $P = 0.015$, $Z = 4.2$, Rayleigh test for non-uniformity; $P = 0.04$ versus shuffled data, see Extended Data Fig. 3). In unpolarized circular environments grid orientations were less clustered than in the square (Fig. 1f; $P = 0.025$, $t = 2.4$, df = 21; two-sample t-test). Clustering did not arise from behavioural biases: the distribution of velocities and directional headings were not different between squares and circles ($P = 0.34$, $t = 0.98$, df = 21 for headings; $P = 0.89$, $t = 0.15$, df = 21 for velocity; two-sample t-test; Extended Data Fig. 4) suggesting that grid patterns align to the walls in polarized enclosures due to the direct influence of environmental geometry and not through changes in behaviour.

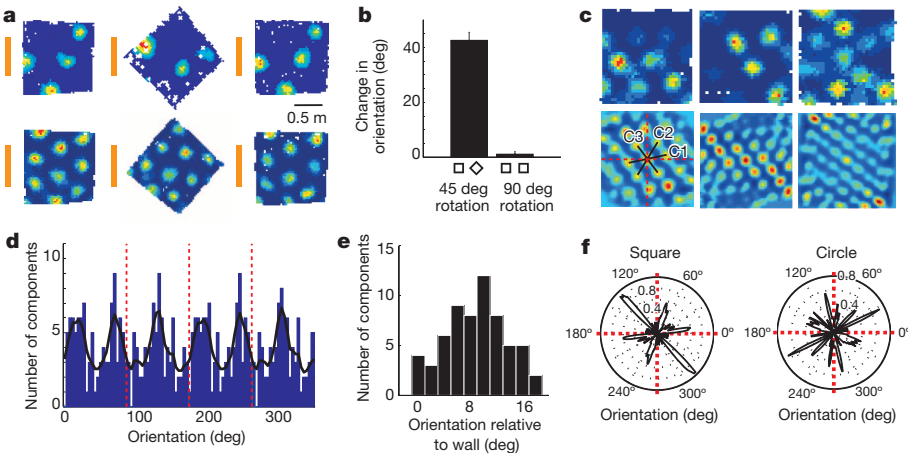

Figure 1 | Grid orientation aligns to walls in squares. **a**, **b**, 45° rotation of a square (middle) rotates the grid pattern by the same amount (2 typical grid cells from 2 rats, distal cue card in orange, $P = 0.44$, $t = -0.85$, $n = 5$, df = 4, one-sample t-test, mean + s.e.m.). **c**, Three typical grid cell rate maps (top) and their spatial autocorrelograms (bottom) ($n = 3$ rats). Orientations of the three main grid components in black, vertical and horizontal walls in red dashed lines. **d**, Distribution of grid orientations for 62 grid modules (41 rats) in squares, **e** is clustered at 8.8° ± 0.6° (mean + s.e.m.) from the vertical or horizontal walls ($P = 0.015$, $Z = 4.2$, Rayleigh test), and **f** is significantly more clustered in square (12 modules) than circle (11 modules) in the same 7 rats ($P = 0.025$, $t = 2.4$, df = 21; two-sample t-test).

[1]Department of Cell and Developmental Biology, University College London, London WC1E 6BT, UK. [2]Sainsbury Wellcome Centre, University College London, London WC1E 6BT, UK.
*These authors contributed equally to this work.

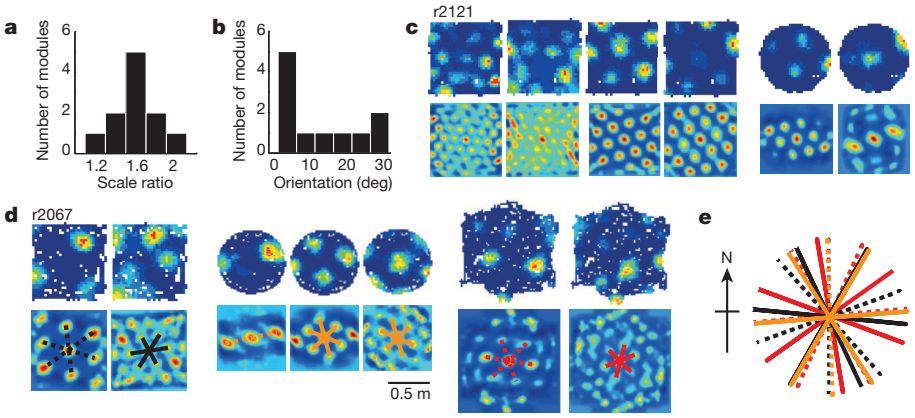

Figure 2 | Relationship between different grid modules across geometrically different enclosures. **a**, Ratio between scales of simultaneously recorded grid modules, mean scale ratio 1.56, $n = 11$ rats. **b**, Distribution of relative orientations of simultaneously recorded grid modules peaks at 0° and 30° but includes intermediates ($P = 0.02$; binomial test). **c**, **d**, Simultaneously recorded grid cells from two different modules maintained their relative orientation in squares, circles and a hexagon. **e**, Preserved relative orientations were not due to the Earth's magnetic field. Colours as in the lower part of **d**. Dashed lines, larger grid modules; solid, smaller scale.

This tendency of grid patterns to orient relative to walls should affect the relative orientations of different grid modules (grid cells cluster into modules differing in orientation and scale)[7,10]. Namely, alignment at ~8.8° to vertical or horizontal walls in a square is compatible only with relative orientations of ~0° or ~30° between modules. Examining data from simultaneously recorded grid modules in the square enclosure (11 pairs, 11 rats, mean scale ratio[7,8,10] between modules 1.56 or ~π/2, Fig. 2a), we found that relative orientations were significantly clustered around 0° and 30° albeit with a few intermediate values (Fig. 2b; $P = 0.02$, binomial test). We asked to what extent the observed clustering across modules was a product of the square environment. Previous reports indicate that grid patterns from different modules can rotate independently[10]. This suggests that in a circle modules will assume relative orientations unrelated to those in a square. Conversely, in a hexagon they should align even if they were aligned to different (vertical or horizontal) walls in a square (Extended Data Fig. 5). Surprisingly, neither was the case. The relative orientation of simultaneously recorded modules was preserved across all three different environmental geometries (square, circle and hexagon; Fig. 2c, d and Extended Data Fig. 5; mean difference in relative orientation across all testing conditions 3.6° ± 2.5°; in 3 rats, 6 modules, 18 cells; $P < 0.001$; binomial test; Extended Data Table 1). Relative alignment by other sensory cues was excluded (enclosures were located in different rooms and animals were disoriented before entering each room), as were non-spatial factors such as the Earth's magnetic field (Fig. 2e). This demonstrates that grid modules located anatomically close together in dorsal medial entorhinal cortex can act coherently.

We next examined whether environmental geometry only affects grid orientation or also impacts other properties such as symmetry, scale and homogeneity. To address this question we recorded the same grid cells in a square and trapezoid, an environment with highly polarized geometry (38 grid cells, 8 rats, 12 modules, Fig. 3a, b). As previously reported[20], grid patterns expanded during initial exposure to the novel trapezoid enclosure (Fig. 3c). To eliminate novelty effects our analyses were limited to data recorded after patterns had stabilized (> 4 days experience; Fig. 3c, d). Interestingly, in the trapezoid even after four days (> 2.6 h of exposure) stable firing fields were 20–30% larger than in the concurrently recorded and equally familiar square (ratio of field diameter in the trapezoid to the square was 1.29, $P = 1.65 \times 10^{-6}$, $t = 14.7$, df = 7; one-sample t-test). Grid patterns also exhibited a permanent decrease in hexagonality (measured by gridness score; Fig. 3e) which resulted from two factors: the pattern was more elliptical across the entire trapezoid (Fig. 3f; mean ± s.e.m. grid eccentricity: 0.67 ± 0.04 (trapezoid) versus 0.55 ± 0.02 (square), $P = 0.02$, $t = -2.5$, df = 22, two-sample t-test) and it was less evenly distributed. To assess the

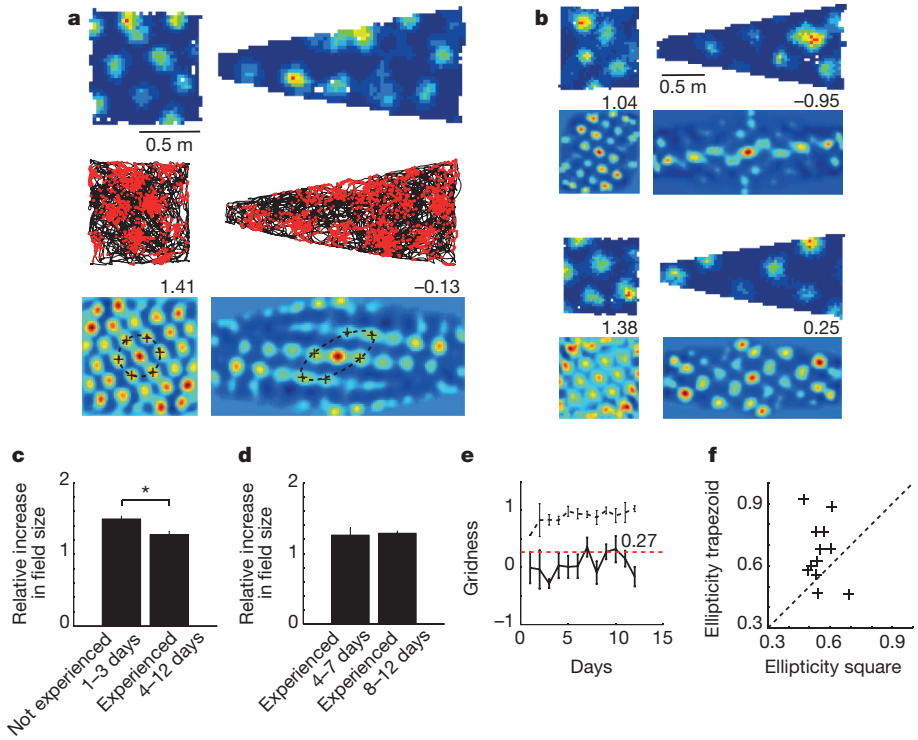

Figure 3 | Grid pattern is distorted in trapezoids. **a**, Grid cell rate maps (top), trajectory (black) with spike positions (red, middle), and spatial autocorrelograms (bottom) for two successive trials in square and trapezoid. Gridness on top right of autocorrelogram. Dashed line, ellipse best approximating grid cell symmetry; '+', main grid components. **b**, Two more examples as in **a** from two other rats. **c**, **d**, Mean ratio between field size in trapezoid and square. Grid fields are larger on days 1–3 than 4–12 (1.49 + 0.04 versus 1.28 ± 0.05 $P = 0.029$, $t = 2.54$, df = 10; two-sample t-test) (**c**) but not significantly different between days 4–7 and 8–12 (**d**) ($P = 0.79$, $t = -0.27$, df = 7, two-sample t-test). **e**, Gridness across days in trapezoid (solid line) and square (dashed line); red line, gridness threshold of 0.27 (ref. 9). **f**, Grid cells are more elliptical in trapezoid than square, mean ± s.e.m.: 0.67 ± 0.04 (trapezoid) versus 0.55 ± 0.02 (square), $P = 0.02$, $t = -2.5$, df = 22, two-sample t-test (all means ± s.e.m.).

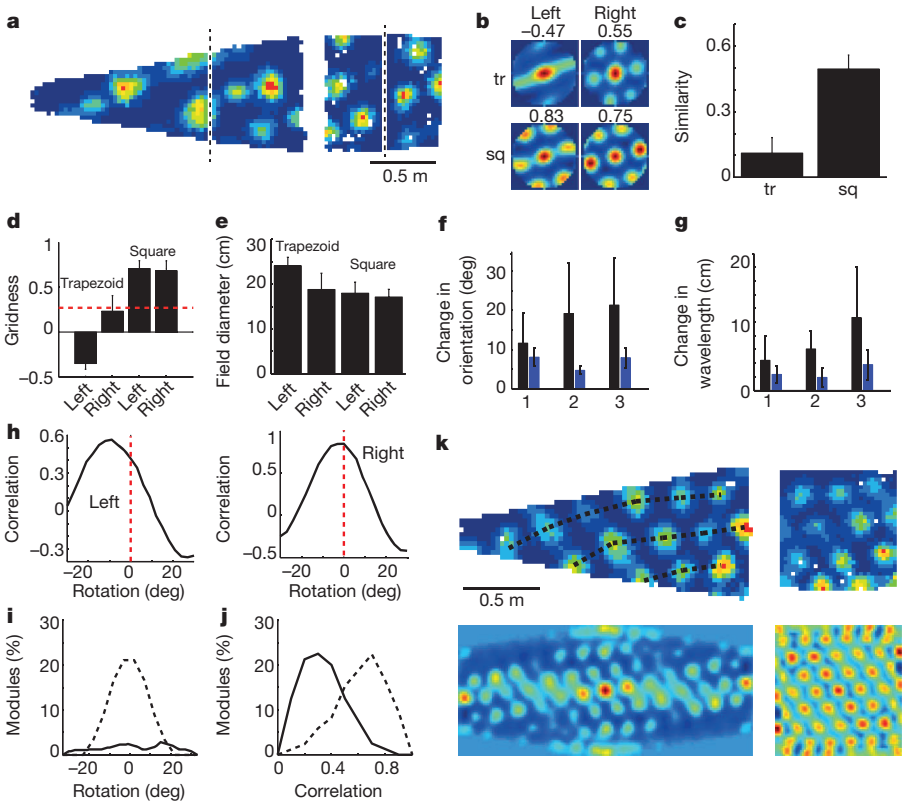

Figure 4 | Grid pattern is inhomogeneous in trapezoids. **a**, Grid cell rate maps for the same cell in trapezoid and square. Dashed line divides enclosures into equal areas. **b**, **c**, Autocorrelograms for each side of the trapezoid (tr) and square (sq) are significantly more similar in the square than the trapezoid (**c**). **d**, Gridness on two sides of the trapezoid and square. Dashed line represents gridness threshold[9]. **e**, Field diameter is larger on the left than the right of the trapezoid ($P < 0.001$, $t = 4.1$, df = 18, two-sample t-test) but not different in the square ($P = 0.39$, $t = 0.88$, df = 18, two-sample t-test). **f**, **g**, Change in orientations (**f**) and wavelengths (**g**) of left/right parts of trapezoid (black) and square (blue). **h**, **j**, Rotation of right part of autocorrelogram relative to left optimizes correlation in trapezoid but not square (**h**) but still leaves a lower similarity (**j**) ($P = 0.0002$, $t = -4.6$, df = 18, two-sample t-test, 32 grid cells, 8 rats, 10 different grid modules). **i**, Average grid rotation between two sides of trapezoid (solid line) and square (dashed line). **k**, Another example of right-to-left grid expansion and rotation in trapezoid. All means ± s.e.m., except for **f**, **g**, which shows means ± s.d.

latter, we divided the trapezoid and square into two equal parts (Fig. 4a; area of half-trapezoid 0.51 m^2, half-square 0.41 m^2) and compared firing on either side. Figure 4b, c shows that the local spatial structure (defined by the spatial autocorrelogram) differs more strongly between the two sides of the trapezoid than between the sides of the square ($r = 0.11 \pm 0.07$ versus 0.50 ± 0.06, trapezoid and square, respectively, $P < 0.001$, $t = -4.0$, df = 18, two-sample t-test, 10 grid modules, 32 grid cells). Moreover, gridness was lower in the left of the trapezoid than the right (Fig. 4d, -0.35 ± 0.07 and 0.23 ± 0.17, respectively, $P = 0.006$, $t = -3.11$, df = 18, two-sample t-test) but not in the square (0.71 ± 0.09 and 0.68 ± 0.11, $P = 0.87$, $t = 0.17$, df = 18, two-sample t-test). Gridness was lower on the right of the trapezoid compared to both parts of the square even though they are of comparable shape and area ($P = 0.009$; $F = 6.18$; two-way ANOVA), suggesting an influence from the left side of the trapezoid. Additionally, the diameters of the individual fields were larger on the left of the trapezoid than the right (Fig. 4e, $P < 0.001$, $t = 4.1$, df = 18, two-sample t-test) but not in the square ($P = 0.39$, $t = 0.88$, df = 18, two-sample t-test). Notably, the field sizes on the right of the trapezoid were not different from those on either side of the square ($P = 0.15$; $F = 2.07$; two-way ANOVA).

We also examined how the orientations and wavelengths of the three grid components computed from the spatial autocorrelogram differed between sides of the two environments (Fig. 4f, g). The orientation of the first component (closest to the horizontal axis; Extended Data Fig. 6) was no more variable between the sides of the trapezoid than the sides of the square (mean orientation change of $11.6^\circ \pm 2.5^\circ$ and $8.0^\circ \pm 0.8^\circ$, trapezoid and square, respectively, $P = 0.19$, $t = -1.36$, df = 16, two-sample t-test). However, the other two components differed more in the trapezoid than in the square (second: $19.2^\circ \pm 4.9^\circ$ and $4.7^\circ \pm 0.3^\circ$ $P = 0.004$, $t = -3.41$, df = 14; third: $21.4^\circ \pm 4.6^\circ$ and $7.9^\circ \pm 0.8^\circ$, $P = 0.005$, $t = -3.3$, df = 14, two-sample t-test). Similarly, the first wavelength was no more variable in the trapezoid than the square (mean wavelength change: 4.4 ± 1.2 versus 2.3 ± 0.4 cm, trapezoid and square, respectively, $P = 0.12$, $t = -1.6$, df = 16, two-sample t-test), while the differences for the second (6.1 ± 1.0 versus 1.9 ± 0.5 cm, $P = 0.001$, $t = -4.1$, df = 14) and third wavelengths (10.1 ± 2.8 cm versus 3.8 ± 0.7 cm, $P = 0.02$, $t = -2.7$, df = 14) were more pronounced in the trapezoid. These localized changes in grid components manifest as a rotation and stretching of the grid pattern across the trapezoid (Fig. 4h–k). Indeed the spatial correlation between the two halves of the trapezoid at the optimal rotation angle (that is, the one maximising the correlation between left and right sides) was still lower compared to the square (Fig. 4h, j; $r = 0.30 \pm 0.05$ trapezoid and 0.63 ± 0.05 square, $P = 0.0002$, $t = -4.6$, df = 18, two-sample t-test), indicating rescaling as well as rotation (Fig. 4k).

To eliminate the possibility that these observations arose from undersampling of the grid pattern in the trapezoid, we generated idealized grid firing (scale and orientation matched to the data) for a square and trapezoid environment (Extended Data Fig. 7). This control data exhibited neither an increase in ellipticity nor in inhomogeneity. Furthermore, although the animals' behaviour was polarized between the two halves of the trapezoid (Extended Data Fig. 4), there was no correlation between the extent of polarization and differences in grid properties between the sides, ruling out a behavioural explanation. Indeed it is known that stereotypical behaviour in the open field does not significantly degrade the hexagonal grid structure[21].

Our results show that most assumptions about the invariant nature of grid cell firing are invalid. In particular the role of environmental boundaries has been underestimated. Our findings reveal that grid patterns are permanently shaped by environmental geometry as well as by internal network processes (Extended Data Figs 8 and 9). Notably, we have shown that grid patterns can be inhomogeneous even within a continuous two-dimensional space, due to the influence of non-parallel boundaries (probably signalled by boundary cells). A differential influence from the boundaries probably also accounts for the ellipticity of different grid modules[10], as well as the non-hexagonal symmetry of spatially periodic non-grid cells[8]. The results challenge the idea that the grid cell system can act as a universal spatial metric for the cognitive map as grid patterns change markedly between enclosures and even within the same enclosure. An intriguing alternative is that grid cells provide a spatial metric but that the asymmetries induced by highly polarized environments such as trapezoids produce distortions in the perception of space.

Online Content Methods, along with any additional Extended Data display items and Source Data, are available in the online version of the paper; references unique to these sections appear only in the online paper.

Received 11 June; accepted 11 December 2014.

1. Hafting, T., Fyhn, M., Molden, S., Moser, M.-B. & Moser, E. I. Microstructure of a spatial map in the entorhinal cortex. *Nature* **436,** 801–806 (2005).
2. Buzsáki, G. & Moser, E. I. Memory, navigation and theta rhythm in the hippocampal-entorhinal system. *Nature Neurosci.* **16,** 130–138 (2013).
3. Fuhs, M. C. & Touretzky, D. S. A spin glass model of path integration in rat medial entorhinal cortex. *J. Neurosci.* **26,** 4266–4276 (2006).
4. Fiete, I. R., Burak, Y. & Brookings, T. What grid cells convey about rat location. *J. Neurosci.* **28,** 6858–6871 (2008).
5. Burgess, N. Grid cells and theta as oscillatory interference: theory and predictions. *Hippocampus* **18,** 1157–1174 (2008).
6. Hasselmo, M. E. Grid cell mechanisms and function: contributions of entorhinal persistent spiking and phase resetting. *Hippocampus* **18,** 1213–1229 (2008).
7. Barry, C., Hayman, R., Burgess, N. & Jeffery, K. J. Experience-dependent rescaling of entorhinal grids. *Nature Neurosci.* **10,** 682–684 (2007).
8. Krupic, J., Burgess, N. & O'Keefe, J. Neural representations of location composed of spatially periodic bands. *Science* **337,** 853–857 (2012).
9. Krupic, J., Bauza, M., Burton, S., Lever, C. & O'Keefe, J. How environment geometry affects grid cell symmetry and what we can learn from it. *Philos. Trans. R. Soc. B* **369,** 20130188 (2014).
10. Stensola, H. *et al.* The entorhinal grid map is discretized. *Nature* **492,** 72–78 (2012).
11. Gallistel, C. *The Organization of Action: A New Synthesis* (Lawrence Erlbaum Associates, 2013).
12. Cheng, K. A purely geometric module in the rat's spatial representation. *Cognition* **23,** 149–178 (1986).
13. Kelly, J. W., McNamara, T. P., Bodenheimer, B., Carr, T. H. & Rieser, J. J. The shape of human navigation: how environmental geometry is used in maintenance of spatial orientation. *Cognition* **109,** 281–286 (2008).
14. Morris, R. G. M., Garrud, P., Rawlins, J. N. P. & O'Keefe, J. Place navigation impaired in rats with hippocampal lesions. *Nature* **297,** 681–683 (1982).
15. O'Keefe, J. & Dostrovsky, J. The hippocampus as a spatial map. Preliminary evidence from unit activity in the freely-moving rat. *Brain Res.* **34,** 171–175 (1971).
16. Taube, J. S., Muller, R. U. & Ranck, J. B., Jr. Head-direction cells recorded from the postsubiculum in freely moving rats. I. Description and quantitative analysis. *J. Neurosci.* **10,** 420–435 (1990).
17. Solstad, T., Boccara, C. N., Kropff, E., Moser, M.-B. & Moser, E. I. Representation of geometric borders in the entorhinal cortex. *Science* **322,** 1865–1868 (2008).
18. Barry, C. *et al.* The boundary vector cell model of place cell firing and spatial memory. *Rev. Neurosci.* **17,** 71–97 (2006).
19. O'Keefe, J. & Burgess, N. Geometric determinants of the place fields of hippocampal neurons. *Nature* **381,** 425–428 (1996).
20. Barry, C., Ginzberg, L. L., O'Keefe, J. & Burgess, N. Grid cell firing patterns signal environmental novelty by expansion. *Proc. Natl Acad. Sci. USA* **109,** 17687–17692 (2012).
21. Derdikman, D. *et al.* Fragmentation of grid cell maps in a multicompartment environment. *Nature Neurosci.* **12,** 1325–1332 (2009).

Acknowledgements We thank J. Poort for discussions. The research was supported by grants from the Wellcome Trust and the Gatsby Charitable Foundation. J.K. is a Wellcome Trust Sir Henry Welcome Fellow. C.B. is a Royal Society and Wellcome Trust Sir Henry Dale Fellow. This work was conducted in accordance with the UK Animals (Scientific Procedures) Act (1986).

Author Contributions J.K. and M.B. planned experiments and analyses. J.K., S.B. and C.B performed the experiments. J.K. and M.B. analysed the data. J.K., M.B., C.B. and J.O'K. wrote the manuscript. All authors discussed the results and contributed to the manuscript.

Author Information Reprints and permissions information is available at www.nature.com/reprints. The authors declare no competing financial interests. Readers are welcome to comment on the online version of the paper. Correspondence and requests for materials should be addressed to J.K. (j.krupic@ucl.ac.uk).

METHODS

A total of 41 adult male Lister Hooded rats were chronically implanted in the left and/or right hemisphere with a microdrive (Axona) loaded with four tetrodes. Tetrodes were aimed at the most dorsal parts of the medial entorhinal cortex (mEC, 39 rats) and adjacent parasubiculum (PaS, 2 rats) (4.3–4.5 mm lateral to the midline; 0.2–0.5 mm anterior to the sinus; angled forwards in the sagittal plane at 0–10° and 1.5 mm below the pia). Tetrodes were lowered 50 μm or less per day at the end of each recording session until the first cells of interest were found. Neural activity was recorded while the animals foraged in square, trapezoidal, circular or/and hexagonal enclosures.

Subjects. A total of 41 adult male Lister Hooded rats were used for the experiments. Rats were individually housed in clear plastic cages (68 cm × 44 cm × 48 cm, W × L × H) and were kept on a 12:12 h light:dark cycle at a controlled temperature (19–23 °C) and humidity (50–70%). The rats weighed 350–450 g on the day of surgery. They were maintained on a 90% of body weight food deprivation schedule where the most recent feeding was at least 12 h before the experiments. Water was supplied ad libitum.

Surgery and electrodes. The rats were anaesthetized with 1–3% of isoflurane in O_2 and a 0.01 mg per 100 g intramuscular injection of buprenorphine. They were chronically implanted in the left and/or right hemisphere with a microdrive (Axona) loaded with four tetrodes (HM-L coated 90% platinum/10% iridium 17 μm diameter wire). The tetrodes were usually tightly glued together and cut at the same level. The electrode tips were plated to reduce the impedance to 150–300 kΩ at 1 kHz. Tetrodes were aimed at the most dorsal parts of the medial entorhinal cortex (mEC, 39 rats) and adjacent parasubiculum (PaS, 2 rats) (4.3–4.5 mm lateral to the midline; 0.2–0.5 mm anterior to the sinus; angled forwards in the sagittal plane at 0–10° and 1.5 mm below the pia). 5–6 screws were threaded into the skull and the microdrive anchored to them with dental cement. A jeweller's screw fixed to the skull over the opposite hemisphere was used as a ground screw. After surgery the rats were given at least 7 days to recover before the experiments were started.

Histology and electrode localization. After completion of the recording sessions the rats were euthanized using an overdose of sodium pentobarbital and perfused transcardially with saline followed by 4% of paraformaldehyde (PFA). The brain was cryoprotected in 4% PFA and 20% sucrose solution and sliced into 30 μm parasagittal sections using a freezing microtome. Sections were mounted and cresyl violet Nissl-stained to allow visualization of the electrode track. Recording sites were determined by measuring backwards from the deepest point of the track and ensuring that the total length of the electrode track corresponded to the amount of electrode movement as measured from the microdrive screw turns (Extended Data Figs 1 and 2). 20% shrinkage was allowed for in histology. mEC layer II cells were identified as a densely packed strongly stained superficial layer of cells. mEC layer III cells were less intensely stained and less densely packed. mEC layer V cells were intensely stained cells in the pyramidal cell layer adjacent to the lamina dissecans. mEC VI layer were less intensely stained and adjacent to layer V. PaS superficial layer cells were identified as densely packed cells located in a dorsal-caudal area above the superficial layers of mEC which showed less staining and did not show a clear laminar structure.

Data collection. Rats were allowed a period of at least 7 days of recovery after surgery at which point screening for cells began. Tetrodes were lowered 50 μm or less per day at the end of each recording session until the first cells of interest were found. Single unit data were acquired using a proprietary data acquisition system (DACQ system, Axona). Two infrared light emitting diodes (LEDs) of different intensities and separated by 7 cm were fixed on the animal's head in order to track the animal's position and head orientation. The (x, y) coordinates of the LEDs were acquired at 50 Hz by an infrared camera attached to the ceiling above the centre of the environment.

Single cell isolation from multi-unit recordings. The experimenter was blind to the cell firing patterns during data collection and cell cluster cutting. Isolation of single units was performed by manual cluster-cutting. Clusters were isolated in a feature space where all possible combinations of pairs of spike amplitudes recorded by four tetrodes were plotted against each other. Unit isolation was further refined by taking into account additional properties of spike waveforms such as the existence of positive pre-potentials. Clusters recorded on different trials were assigned to the same cell if: (1) the tetrode had not been moved between trials; (2) there was minimal change in spike waveforms; (3) the position of the target cluster and neighbouring clusters remained similar in feature space. Despite having been recorded on several trials however, each cell was only included once in any analysis reported in this paper.

Training procedures and testing environments

Square enclosures. Cells were recorded as the animals foraged in one of a number of familiar square enclosures of the following dimensions (L × W × H): 0.6 m × 0.6 m × 0.5 m; 0.9 m × 0.9 m × 0.5 m; 1 m × 1 m × 0.5 m; 1.2 m × 1.2 m × 0.5 m; 1.3 m × 1.3 m × 0.5 m; 1.6 m × 1.6 m × 0.5 m; 1.9 m × 1.9 m × 0.5 m. The recording enclosures were always placed in the same position with respect to the laboratory during training and testing sessions. Distal visual cues (for example, a white rectangular cue card, shelves, recording system etc.) were available to maintain the same allocentric directional sense across sessions. The animals were trained to forage for sweetened rice thrown into random locations in the enclosure approximately every 10–20 s. At least two 15 min trials were recorded within a day. There were 10 min intervals between every trial during which the animal rested on a holding platform located near the testing environment.

Circular enclosures. Cells were also recorded in 9 animals in a 0.8 m diameter × 0.5 m high circular enclosure located in a different unfamiliar room. The animals had at least 6 training sessions over a three-day period before testing. Training and testing were performed with black curtains around the recording circle and the only available landmark was a large well-illuminated white cue card (0.8 m × 1.2 m). The animals were disoriented before each session by slowly walking in the corridor and rotating the enclosed animal carrying box at ~0.1 Hz. Each session included two trials (10 and 15 min) with ~5–10 min break between them during which the animal rested in his carrying box inside the curtained environment.

Trapezoidal enclosures. Cells were also recorded in 8 animals in an isosceles trapezoidal enclosure (lengths of the shorter and longer parallel walls were 0.2 m and 0.9 m, respectively, with angled walls equal to 1.9 m; 0.5 m height). Each recording session consisted of 5 trials: (a) the first 8–10 min trial in a 0.9 m^2 square; (b) 15 min trial in the square; (c, d) 20 min trial in the trapezoid; (e) 15 min in the square. The animal had ~10–15 min breaks between trials. The animals were not disoriented between the trials. The square and the trapezoid were centred at the same position in the room below the tracking camera. The room was well illuminated with multiple cues positioned around the recording enclosures including one large well-illuminated white card (1.13 m × 0.83 m) at the west side of the environment. Initial cell screening was carried out in the square enclosure until the first location-modulated cells were recorded and then the training in the trapezoid was begun. In two rats grid cells were recorded from the first exposure to both the square and the trapezoid to investigate the time course of scale changes with response to novelty and subsequent familiarization.

Hexagonal enclosure. Two animals were also recorded on a familiar hexagonal platform (with length of each side equal to 0.83 m) located in a third different experimental room. The hexagonal platform had no walls and was located in an environment with many visible visual cues.

All the first trials of the day (that is, trial 'a') were excluded to minimise novelty effects.

Firing rate maps. A locational firing rate map was estimated by dividing the number of spikes fired in a given part of the environment by the time spent there. Position data and spike counts were sorted into 2.5 cm × 2.5 cm spatial bins. Unsmoothed firing rate maps were obtained by dividing the spike count in each bin by the dwell time in that bin. The smoothed firing rate map was obtained by first applying adaptive smoothing (see adaptive smoothing section) to the dwell time and spike maps and then dividing them. Colour bars represent firing rate in deciles of the range of firing rates (top 10% in red, bottom 10% in blue). Unvisited bins are shown in white.

Directional firing rate was estimated by dividing spike counts and dwell times into 3 degree bins. Adaptive smoothing was applied to spike and dwell time maps before dividing them.

Adaptive smoothing. Adaptive smoothing[22] was applied to the firing rate maps. In brief, to calculate the firing rate for a given bin the number of spikes assigned to that bin is defined by a circle centred at the bin with the radius r. The radius of the circle is expanded until:

$$r \geq \frac{\alpha}{n\sqrt{s}}, \quad (1)$$

where $\alpha = 5{,}000$, n is the number of bins and s is the number of spikes lying within the circle.

Criteria for cell classification. Grid cells were identified by comparing the gridness score to a threshold value calculated as the 95th percentile value of shuffled data. The data was shuffled following ref. 23 by wrapping the time-shifted spike train around the position data. The spike train was shifted by a random duration more than 20 s and less than the trial duration minus 20 s. Each shuffling procedure was performed 200 times to estimate the gridness threshold. Grid cells were classified based on their gridness score in the square.

Identifying grid cells. Gridness was obtained as in ref. 24. We calculated the spatial autocorrelogram as:

$$r(\tau_x,\tau_y) = \frac{n\sum f(x,y) f(x-\tau_x, y-\tau_y) - \sum f(x,y)\sum f(x-\tau_x, y-\tau_y)}{\sqrt{n\sum f(x,y)^2 - \left(\sum f(x,y)\right)^2}\sqrt{n\sum f(x-\tau_x, y-\tau_y)^2 - \left(\sum f(x-\tau_x, y-\tau_y)\right)^2}} \quad (2)$$

where $r(\tau_x, \tau_y)$ is the autocorrelation between bins with spatial offset τ_x and τ_y. f is the firing rate map of the cell with no smoothing applied, n is the number of overlapping bins in two offset copies of the map. The autocorrelogram was smoothed

using a two-dimensional Gaussian kernel of 5 bins with standard deviation equal to 2 bins. The six local peaks of the autocorrelogram were defined as the six local maxima with $r > 0$ closest to the central peak (excluding the central peak itself). Gridness was calculated by defining a mask on the spatial autocorrelogram centred on the central peak but excluding the peak itself bounded by a circle defined by the mean distance from the centre to the closest peaks multiplied by 2.5. This area was rotated in 30 degrees increments up to 150 degrees and for each rotation the Pearson product-moment correlation coefficient was calculated against the un-rotated mask. Gridness is then calculated taking the difference between the minimum correlation coefficient for rotations of 60 and 120 degrees and the maximum correlation coefficient for rotations of 30, 90 and 150 degrees.

The field size and orientation of the grid cells. The local spatial autocorrelogram was used to estimate grid cell orientations and the average field size. The local spatial autocorrelogram is defined as a central part of spatial autocorrelogram which includes six nearest peaks around the central peak. The orientations of all the six peaks were estimated as the angles between the horizontal central axis and the line traversing the central peak and a surrounding peak (six orientations for all the six surrounding peaks) in an anti-clockwise direction.

The average field size was calculated using the diameter of the central field. The area of the central field was estimated as a sum of all the conjunctive bins within the centre fields after 20% threshold was applied.

Grid cell ellipticity. Grid ellipticity in trapezoids and squares was assessed by fitting an ellipse to the six central peaks of the local spatial autocorrelogram using a least squares method. Eccentricity e was used as a measure of ellipticity (with 0 indicating a perfect circle)[25,26]:

$$e = \sqrt{1 - \frac{b^2}{a^2}} \quad (3)$$

where b and a are the lengths of the smaller and longer axes of the ellipse respectively.

Grid cell orientation clustering in square enclosures. We identified all the grid cells recorded in each animal in a familiar square enclosure. When the same grid cell was recorded on more than one trial, the data from only one trial, chosen at random, was used. Eighteen animals had two different grid modules and one animal had three different grid modules. The average orientations from each module were calculated and displayed (Fig. 1d). We estimated the average deviation of grid orientation from the closest wall (vertical or horizontal) for each module (Fig. 1e).

We tested the degree of grid orientation clustering in the square by comparing the values of normalized Fourier power of the circular autocorrelogram of measured orientation distribution (Fig. 1d) versus the distribution where the grid orientations were rotated by a random amounts. Circular autocorrelogram was calculated with the bin size of 2° (Extended Data Fig. 3a). Only half of autocorrelogram was included for Fourier analysis (that is, from 0° to 180°) as the other half is symmetrical. The autocorrelogram was zero-padded from 90 bins to 2^{13} bins to enhance the resolution of the one-dimensional Fourier spectrogram. A large peak was observed at 3 Hz indicating clustering at 60° (Extended Data Fig. 3b). To test the possibility that the observed clustering could occur by chance, 10,000 shuffle sets were produced. In each shuffle a random direction was generated for each module and added to all three directions of the respective module to preserve the relative orientations. In each instance the one-dimensional Fourier spectrogram was calculated under the same condition as for the unshuffled data. The ratio of power within peak at 3 ± 1 Hz and total power (from 0 to 45 Hz) was calculated (called the normalized Fourier power) and compared with the same measure for unshuffled data. The hypothesis that clustering at 60° could be observed by chance was rejected with $P = 0.0438$ (Extended Data Fig. 3c).

We also assessed how significant grid orientation clustering is in squares by comparing it against orientation clustering in a circle for the same 7 animals recorded in squares (12 modules) and circles (11 modules). If the geometry of the environment affects grid orientation, the clustering of orientations should be more variable in circles compared to squares. To test for clustering of orientations we found the distribution of three orientations modulo 60° (the other three are symmetrical to the former ones) and compared whether standard deviations of these distributions were significantly different in squares versus circles using a two-sample t-test.

Comparing behavioural biases in square versus circular enclosures. We examined whether differences in grid cell firing patterns in squares versus circles could be explained by systematic differences in directional and velocity profiles. To identify biases in the directional (or velocity) sampling of the environment we introduce a circularity score which is equal to the sum of squared distances between the measured sampling distribution and a perfect circle with radius equal to the mean of the sampling distribution.

$$m = \sum_{i}^{n} (r_i - \bar{r})^2 \quad (4)$$

Here m is the circularity score, r_i is a mean value in a bin i, $\bar{r}$ is mean value and n is number of bins (where r can be direction or velocity). In order to compare directional sampling between trials with different duration, m was normalized by n^2.

We calculated circularity scores for all trials with grid cells included in the current analysis (Extended Data Fig. 4). The average score was calculated for each module. A two-sample t-test was used to compare the degree of circularity.

Defining grid cell modules. A grid cell module was defined as a group of anatomically neighbouring grid cells which had similar scale and orientation[25].

Testing whether relative orientations between different grid modules are preserved across different testing conditions. We looked at 18 grid cells (3 rats, 6 modules in each rat) recorded in up to three different environments (Fig. 2c–e and Extended Data Fig. 5). The relative orientation is defined as the mean orientation difference between closest components of two simultaneously recorded modules. We asked if these modules kept their relative orientation across different testing arenas, that is, the difference between the corresponding relative orientations should be close to zero. To test this we calculated the mean difference between the relative grid orientations in the square and in another testing environment (a circle or a hexagon; Extended Data Table 1) and estimated how likely it is to get such a mean difference by chance applying the binomial test (the range of available differences is 0°–30°).

Non-homogeneity of grid cell firing pattern in trapezoids. We examined how homogeneous the grid cell firing pattern is in trapezoids versus squares. To measure homogeneity we divided the enclosures into two parts (left and right) with equal areas (in the case of the trapezoid its horizontal axis is divided into segments 64% and 36% of the whole). We calculated local spatial autocorrelograms for the left and right parts of the trapezoid and square separately. To evaluate the degree of similarity between the left and the right parts of the environment (square or trapezoid) we calculated the Pearson product-moment correlation coefficient between them. If the sizes of local spatial autocorrelograms were different between the different parts, the larger was cropped to the size of the smaller one. We also calculated the gridness score for each of them.

The orientation and scale on the left and right sides of the trapezoidal and square enclosures were evaluated from the local spatial autocorrelogram of each side (see the section on field size and orientation of the grid cells for details). The components closest to the horizontal axis were considered the first grid cell component, the second component was that at the closest angle in anti-clockwise direction followed by the third (Extended Data Fig. 6).

Anisotropy of grid firing pattern in the trapezoid does not result from inadequate behavioural sampling. To examine whether the changes in grid cell properties on the left part of the trapezoid resulted from inadequate behavioural sampling of the left side, we generated a perfect homogeneous grid pattern in a square which had the same wavelength and orientation as grid cells recorded in the square environment as estimated from the six peaks of the local spatial autocorrelogram (Extended Data Fig. 7). We then transposed this idealized pattern onto the trapezoidal shape and measured the similarity and gridness of the left and right parts of the trapezoid and found no difference in gridness, demonstrating that the differences seen in the real data are not due to inadequate sampling on the left side of the trapezoid. We also found the orientations and wavelengths of the main three grid components of simulated grid patterns in the left and right sides of a trapezoid and a square and showed that they had much smaller differences than observed in our data and that they were not different across different directions.

Change in symmetry cannot be simply predicted by morphing the pattern from a square to a trapezoid. We tested whether the observed change in symmetry of grids recorded in a trapezoidal enclosure can be predicted by the simple morphing of the pattern from a square to a trapezoid (Extended Data Figs 8 and 9). To estimate how grid pattern in a square would appear in a trapezoid, we expanded the initial grid pattern in the square into a larger square with the length equal to the long length of the trapezoid. Then we rescaled the pattern along the horizontal trapezoid axis to match the size of the original trapezoid (similar to ref. 26). The correlation coefficients between the predicted versus recorded grid patterns were used to estimate how well our transformation matched the experimentally measured pattern. The distribution is not significantly different from the normal distribution with a mean equal to zero ($P = 0.74$, $t = -0.33$, $df = 36$, one-sample t-test).

Comparing behavioural biases in the left part of the trapezoid versus the right. We used the same analysis as described in the section entitled comparing behavioural biases in square versus circular enclosures for comparing the sampling bias on the left side of the trapezoid with that on the right. We divided the trapezoid into two equal parts (area of half-trapezoid, 0.51 m^2) and calculated the directional and velocity circularity scores for each part. A two-sample t-test revealed that on the whole both directional and velocity sampling distributions were different between the two parts (Extended Data Fig. 4). We then measured the correlation between the degree of similarity of the local grid pattern and the difference in sampling biases on the left and the right sides (Extended Data Fig. 4e, f). We showed that there is no

significant correlation between these measures suggesting that observed grid non-homogeneity in the trapezoid did not result from the difference in directional or velocity sampling distributions.

22. Skaggs, W. E., McNaughton, B. L., Gothard, K. M. & Markus, E. J. *An Information-Theoretic Approach to Deciphering the Hippocampal Code* 1030–1037 (Morgan Kaufmann, 1993).
23. Wills, T. J., Cacucci, F., Burgess, N. & O'Keefe, J. Development of the hippocampal cognitive map in preweanling rats. *Science* **328,** 1573–1576 (2010).
24. Hafting, T., Fyhn, M., Molden, S., Moser, M.-B. & Moser, E. I. Microstructure of a spatial map in the entorhinal cortex. *Nature* **436,** 801–806 (2005).
25. Stensola, H. *et al.* The entorhinal grid map is discretized. *Nature* **492,** 72–78 (2012).
26. Barry, C., Hayman, R., Burgess, N. & Jeffery, K. J. Experience-dependent rescaling of entorhinal grids. *Nature Neurosci.* **10,** 682–684 (2007).

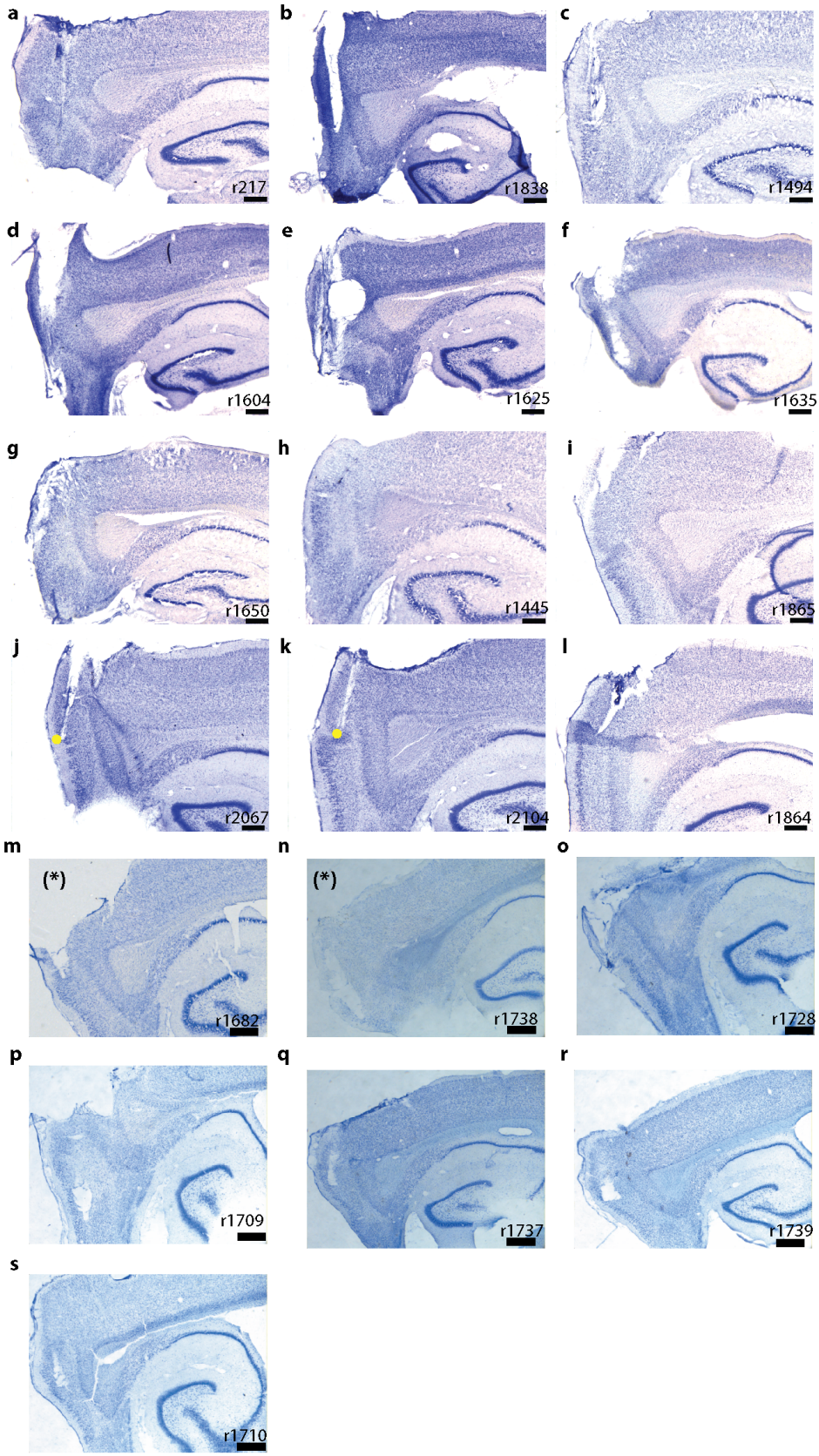

Extended Data Figure 1 | Sagittal Nissl-stained brain sections showing the recording locations in superficial layers II-III of mEC and PaS. **a–s**, Yellow dots indicate the dorsal-ventral region where grid cells were recorded in the trapezoids. PAS marked with asterisk symbols. Scale bar, 500 μm.

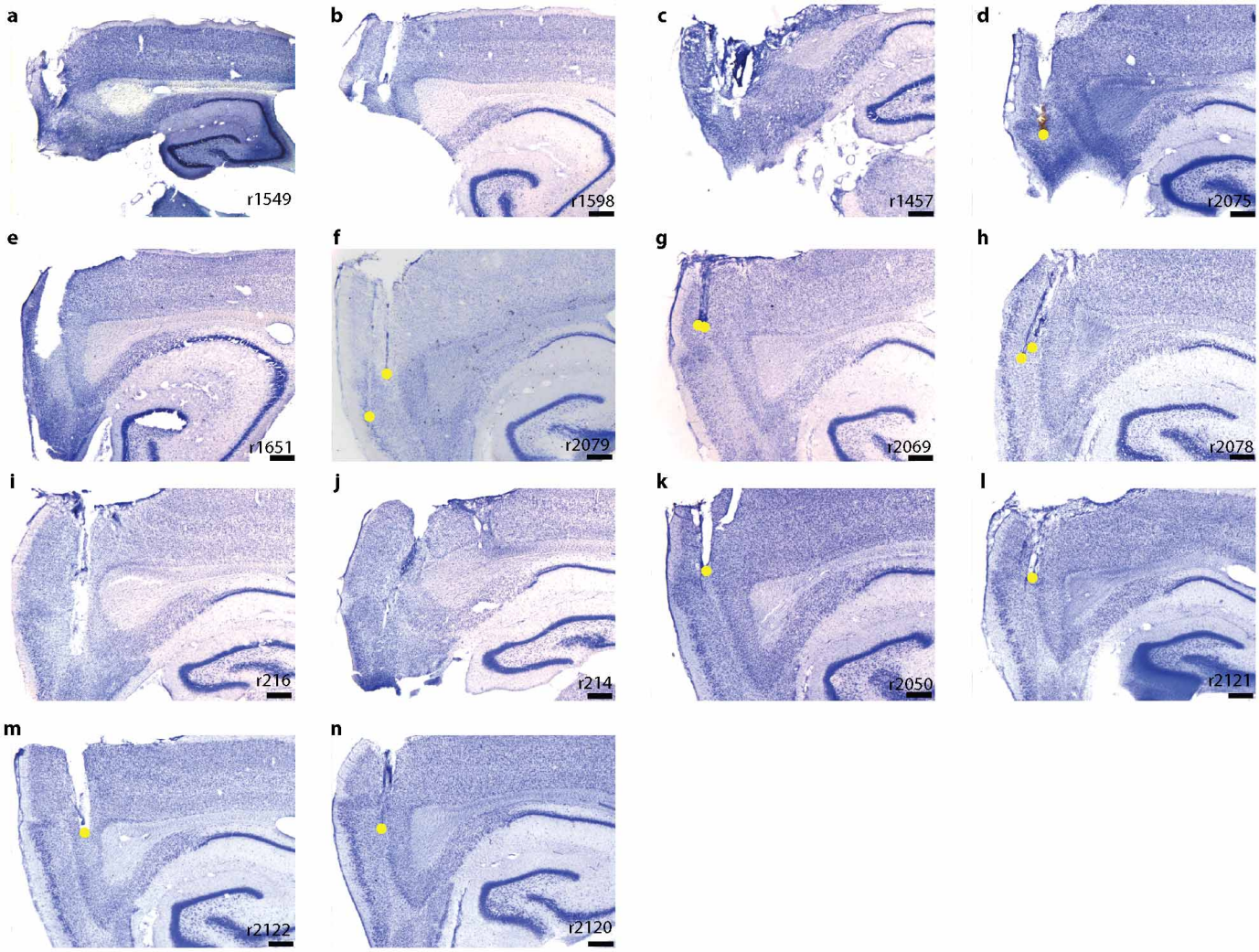

Extended Data Figure 2 | Sagittal Nissl-stained brain sections showing the recording locations in superficial II–III and deep V–VI layers of mEC. **a–n**, Yellow dots indicate the dorsal-ventral region where grid cells were recorded in the trapezoids. Scale bar, 500 μm.

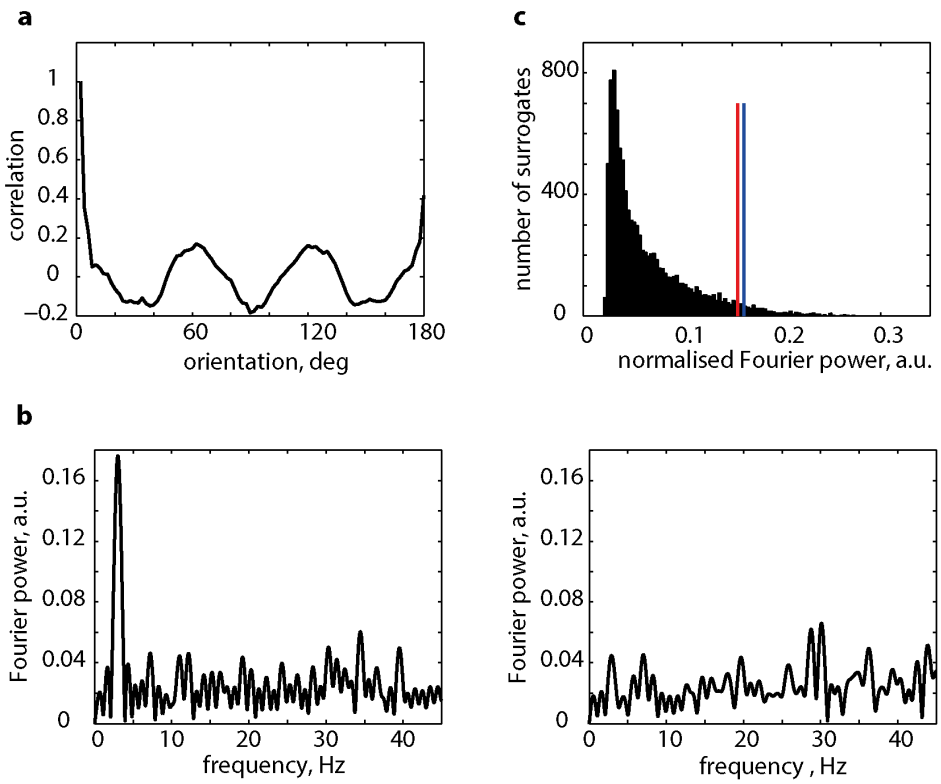

Extended Data Figure 3 | Orientation clustering. **a**, The autocorrelogram of the distribution of grid orientations in squares (shown in Fig. 1b). **b**, The Fourier spectrogram of autocorrelogram in **a**, left, and a typical example of the Fourier spectrogram of the autocorrelogram of shuffled orientations, right. Note the absence of a low-frequency peak in the latter. **c**, The distribution of maximum normalized Fourier power of 10,000 data surrogates (as shown in **b**, right). Red line indicates 95 percentile of the shuffled data. Blue line indicates the maximum normalized Fourier power of our data.

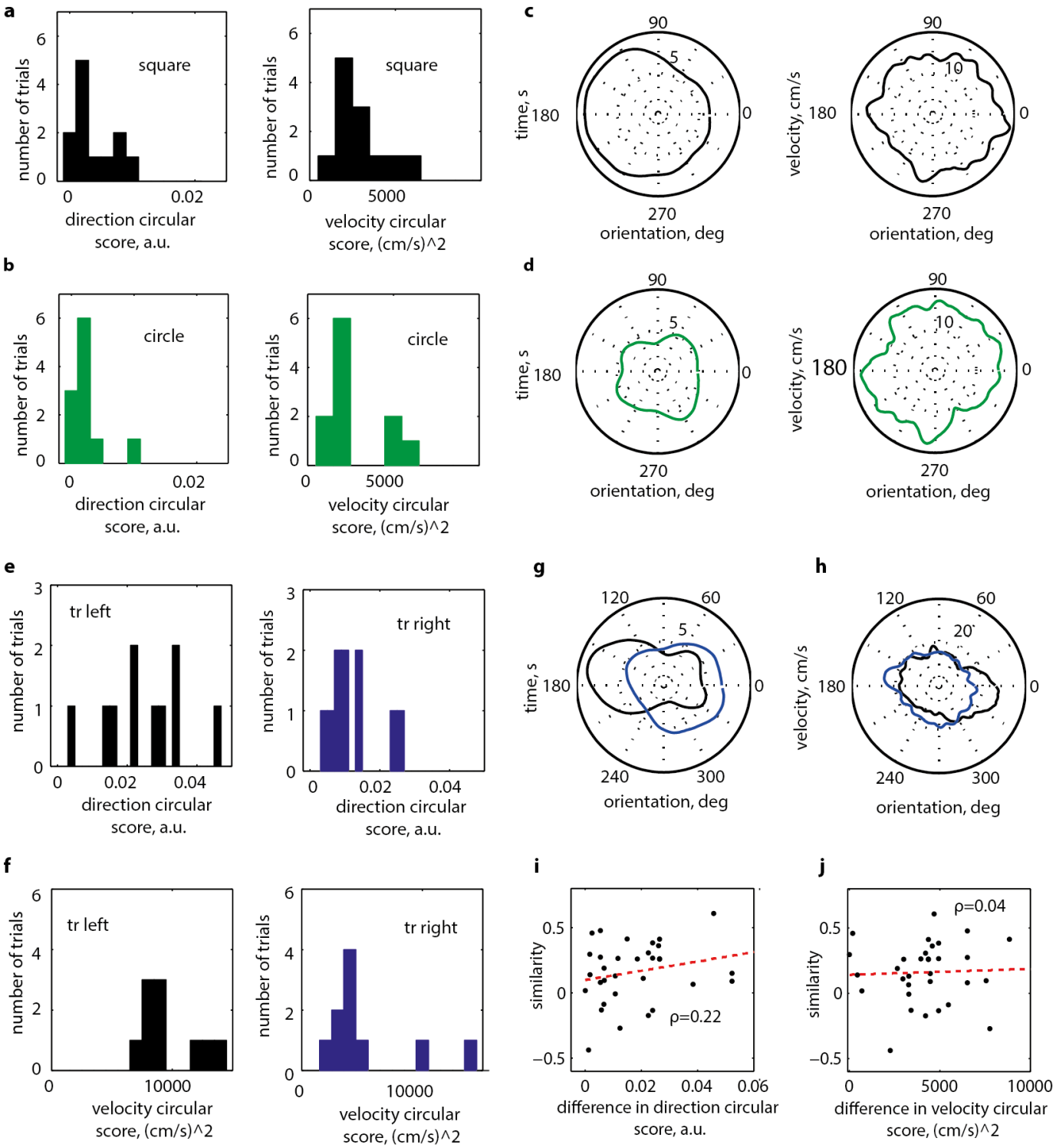

Extended Data Figure 4 | Directional and velocity sampling in square and circular enclosures. **a**, **b**, Mean directional (left) and velocity (right) sampling in square (**a**) and circular (**b**) enclosures. **c**, **d**, Typical examples of directional (left) and velocity (right) sampling profiles in square (**c**) and circle (**d**). **e**, Directional sampling in the left (left, black) and right (right, blue) parts of the trapezoid. The directional sampling in the left part of the trapezoid was significantly more biased than in the right ($P = 0.01$; two-sample t-test; means ± s.e.m. = 0.025 ± 0.004 (left) and 0.012 ± 0.002 (right). **f**, The velocity sampling bias was also significantly larger in the left part of the trapezoid (left, black) than the right (right, blue) ($P = 0.006$; two-sample t-test; mean velocity sampling ± s.e.m. = 9,803 ± 791 $(cm/s)^2$ (left) and 5,413 ± 1,176 $(cm/s)^2$ (right). **g**, **h**, Typical examples of the directional sampling (**g**) and velocity sampling (**h**) on the 2 sides of the trapezoid; rat 2104. The left side trapezoid direction circular score is 0.035 (black), the right, 0.009 (blue). The left side trapezoid velocity circular score is 8,268 $(cm/s)^2$ (black) and the right, 3,904 $(cm/s)^2$ (blue). **i**, **j**, Absence of a significant correlation ρ between the similarities of the left and right sides of the trapezoid and the difference in directional (**i**), $P = 0.22$ or velocity (**j**) scores, $P = 0.82$.

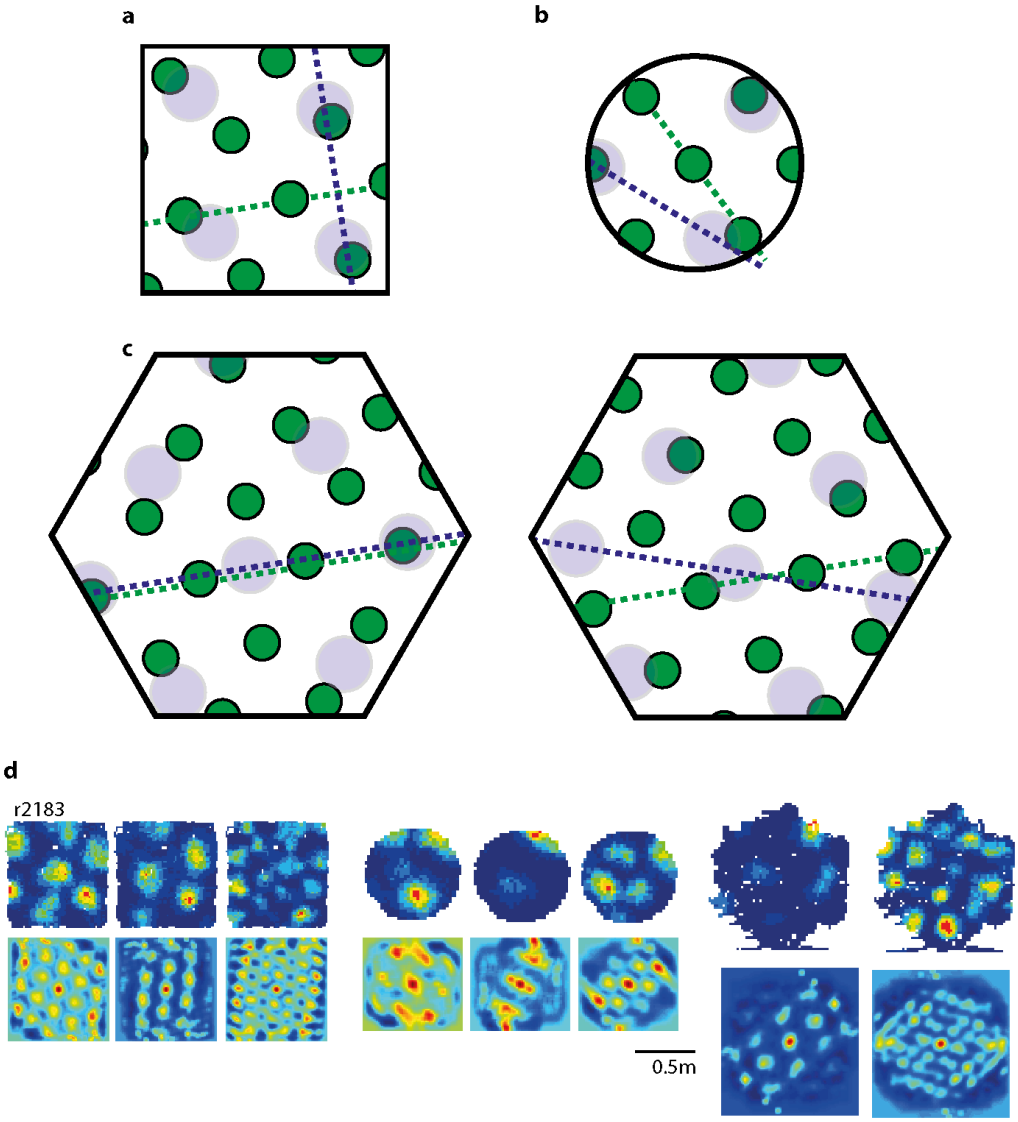

Extended Data Figure 5 | Schematic representation of grid re-alignment in different shape enclosures. **a**, The relative orientation of two representative grid modules in a square. The grid cell with the smaller scale (green) is aligned ~9° from the horizontal wall and the grid cell with the larger scale (blue) is aligned ~9° from the vertical wall with the relative orientation between them equal to 30°. **b**, If grid cells respond independently and if the geometry of the environment determines their orientation in non-polarized environments such as a circular enclosure, grid cells in **a** should randomly realign (in the current example by ~15°). **c**, Similarly, in the hexagonal enclosure both grid cells should start to align (left) or become ~18° offset from each other (right). This was not observed in our experimental data. **d**, Simultaneously recorded grid cells from two different modules (rat r2183) in a square (left), a circle (middle) and a hexagon (right) maintained their relative orientation. Rate maps are shown on the top row and spatial autocorrelograms on the bottom.

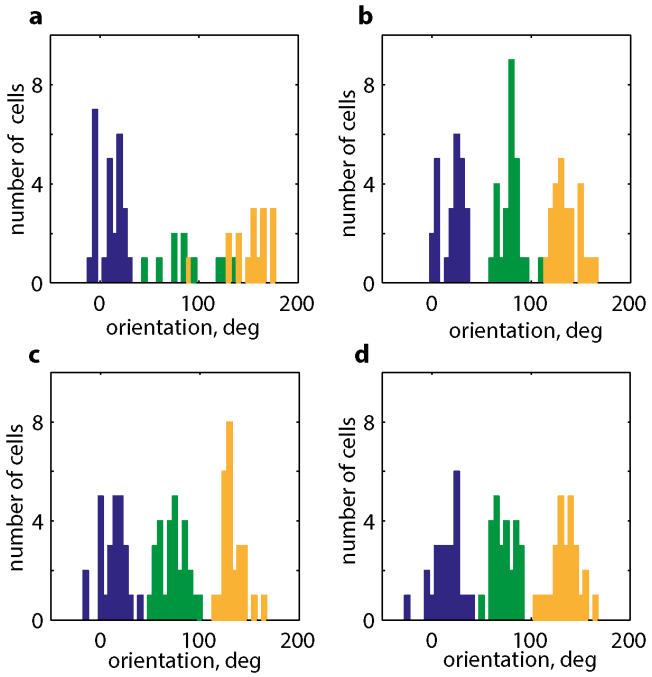

Extended Data Figure 6 | Distribution of grid components on the left and right sides of trapezoidal and square enclosures. a–d, The distribution of the individual grid cell components on the left (**a**) and right (**b**) sides of the trapezoid and square (left (**c**) and right (**d**)). Components 1, 2 and 3 are shown in blue, green and orange, respectively. Data from 8 rats, 10 grid modules, 26 grid cells. Note the similarity of all 4 blue components and of the green and orange components on both sides of the square and on the right side of the trapezoid.

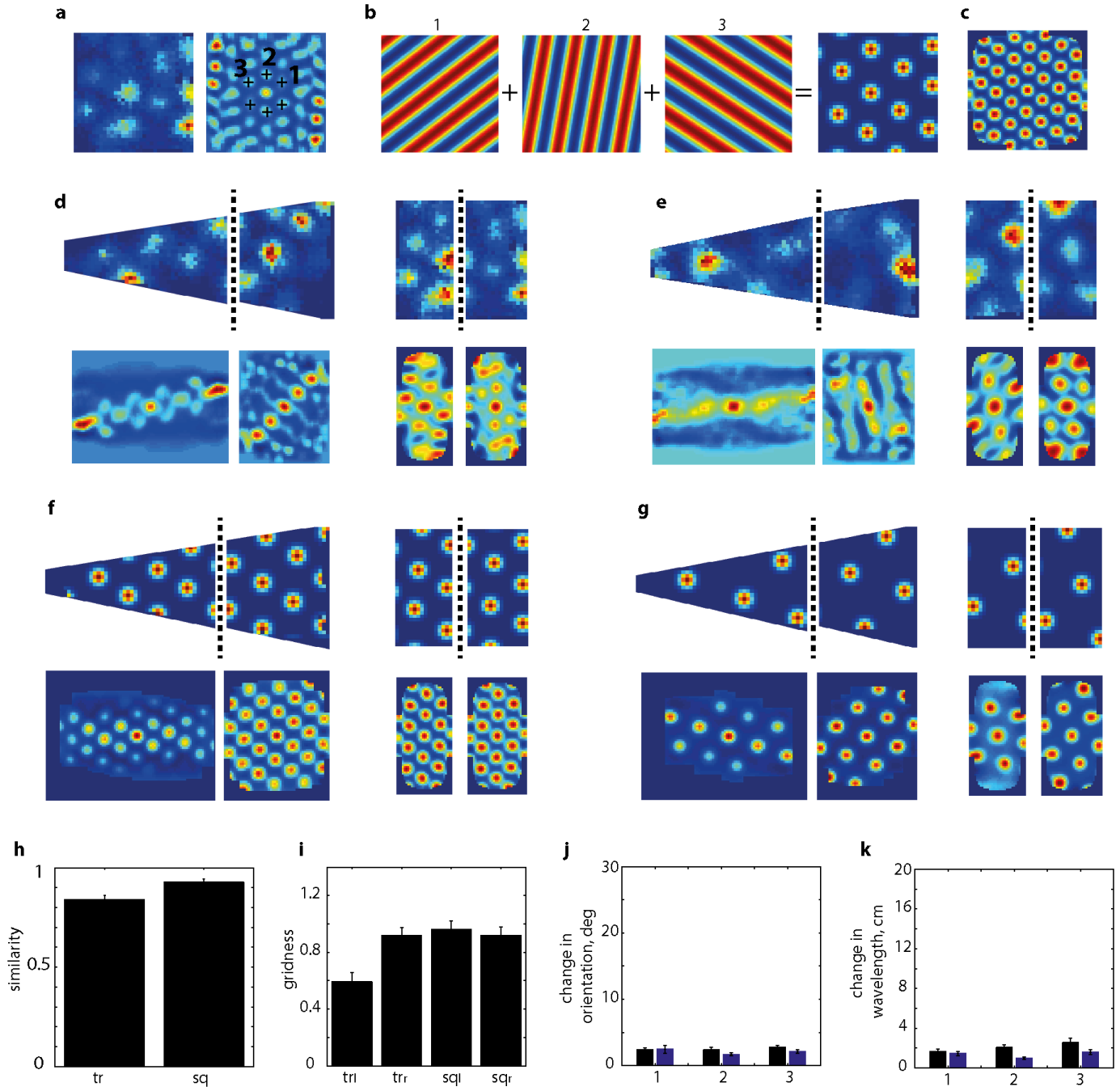

Extended Data Figure 7 | Simulated grid cells. **a**, Grid cells were simulated using the orientations and wavelengths of the three main grid components (1, 2, 3) taken from the spatial autocorrelogram (**a**, right) of a real grid cell (**a**, left) as shown in this typical example. **b**, Simulated grid pattern was generated by summing three grid components to retrieve the rate map and spatial autocorrelogram (**c**) which well approximated the real data shown in **a**. **f**, **g**, examples of the procedure applied to the two cells in **d** and **e**, respectively. Grid cells were generated from the autocorrelogram in the square. **h**, Correlation coefficient between right and left side of the simulated grid data in trapezoid (left) and square (right). **i**, Grid scores of simulated grids on left and right side of trapezoids and squares. The lower grid score in the left side of the trapezoid is due to under-sampling. **j**, **k**, Change in orientation (**j**) and wavelength (**k**) of 3 components of simulated grids in trapezoid (black bars) and square (blue bars). All means ± s.e.m.

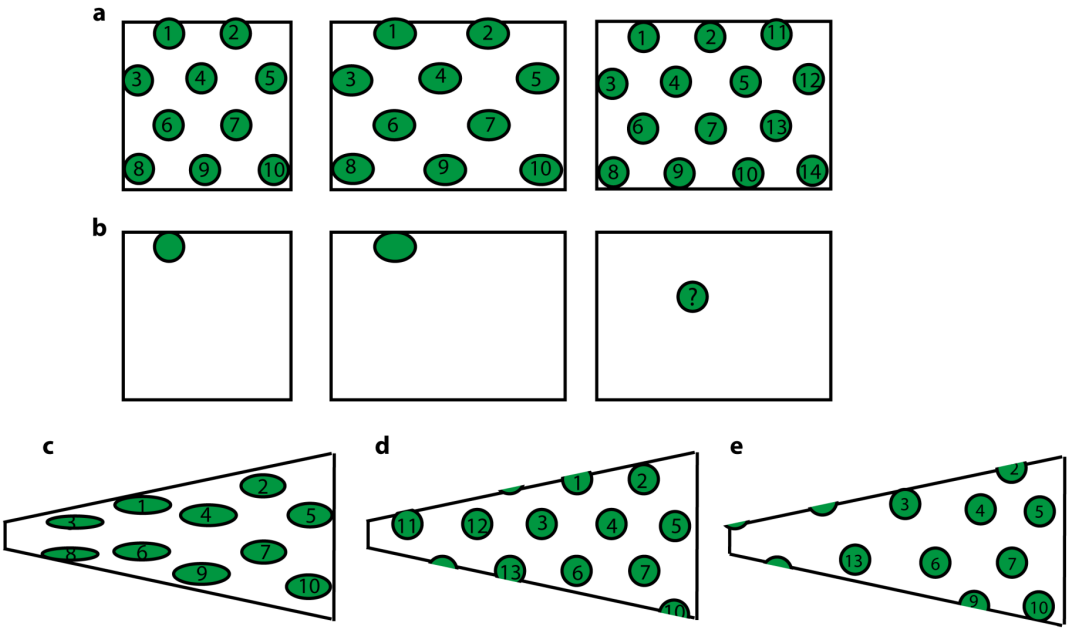

Extended Data Figure 8 | Temporary rescaling versus permanent change in grid symmetry. **a**, Expected rescaling of a grid cell (left) in a rectangle (middle). The number of grid fields stay the same ($n = 10$ fields) but the fields become more elliptical and farther apart along the x direction. After a few days of experience the fields converge to their initial size and shape, and the number of grid fields increases (right). The grid symmetry on the left and right belong to the same sixfold symmetry group (that is, hexagonal symmetry). **b**, Place cell response to rescaling of the environment. The place field initially becomes more elliptical (middle) and finally remaps to a random location (or stops firing altogether) as the animal becomes more experienced. **c**, Expected change in grid symmetry as the animal goes from square (**a**, left) to trapezoid if the change in pattern occurred due to the rescaling of the environment. Note that the number of fields remains unchanged. **d**, As the environment becomes more familiar the grid cell pattern should converge to hexagonal symmetry and the number of fields would increase. In general we did not observe this in our data. **e**, Instead, grid symmetry became more elliptical (not grid fields) and the scale increased towards the narrow side of the trapezoid.

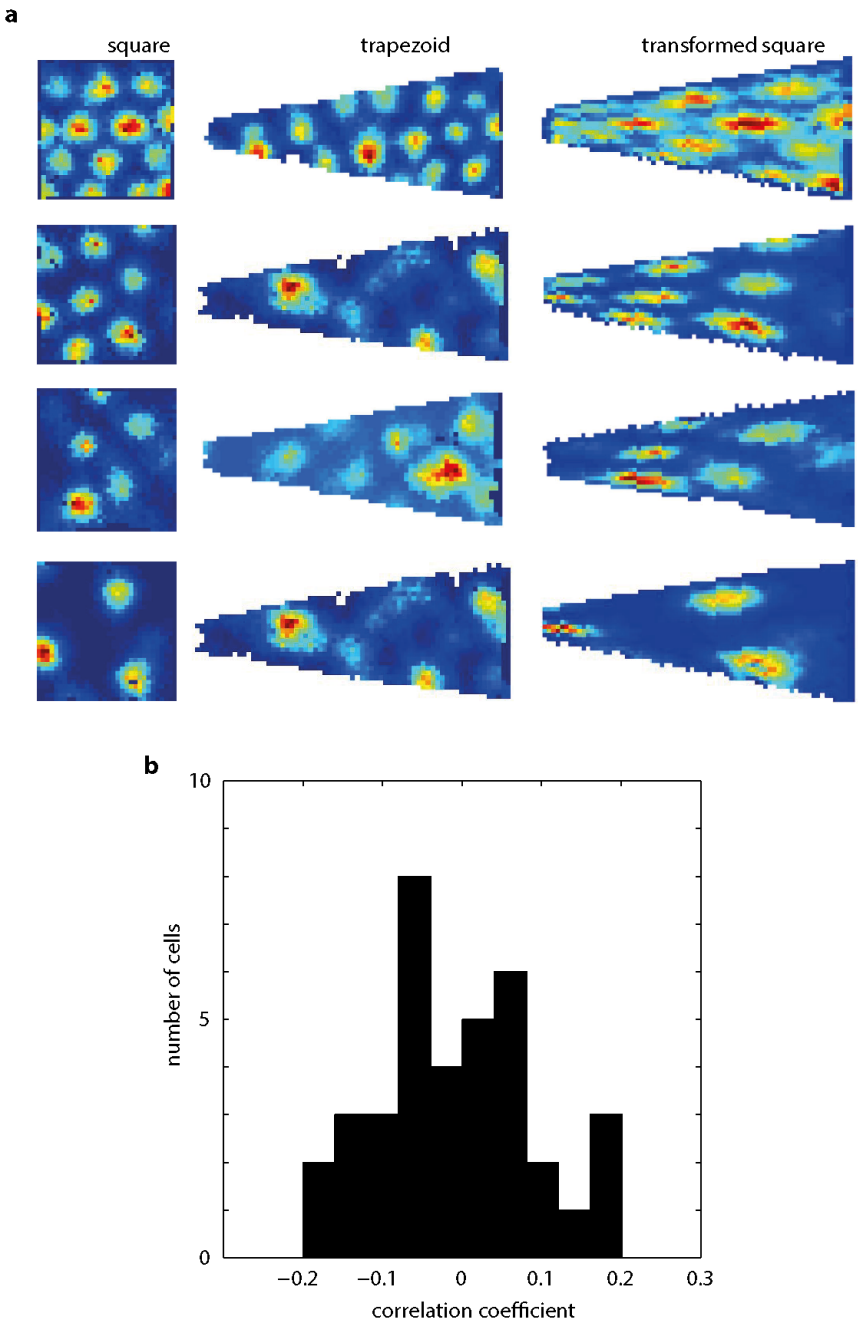

Extended Data Figure 9 | Grid cell pattern in trapezoid cannot be predicted by a simple transformation of a square to a trapezoid. **a**, Panel shows 4 grid cells from 4 rats recorded in a square (left) and trapezoid (middle). Predicted grid pattern (right) obtained by transforming a grid recorded in a square (left) into a trapezoid. **b**, Correlation coefficients between the predicted morphed grid pattern and the one actually recorded in the trapezoid. The distribution is not significantly different from the normal distribution with a mean equal to zero ($P = 0.74$, $t = -0.33$, df = 36, one-sample t-test).

Extended Data Table 1 | The main grid cell properties in hexagonal, square and circular enclosures

Rat No	Grid cell No	Grid Module No	Environment	Grid scale, cm	Grid orientation axis1, deg	Grid orientation axis2, deg	Grid orientation axis3, deg	Relative grid orientation between module1 and module2
2067	1	1	Hexagon	60	46.6	110.9	170.9	
2067	2	2	Hexagon	42	16.4	76.8	132.3	25.7
2067	3	1	Square	55	36.4	95.7	161.6	
2067	4	2	Square	35	11.3	53.1	121.0	23.9
2067	5	1	Circle	77	13.3	-	-	
2067	6	2	Circle	58	45.0	106.9	159.1	
2067	7	2	Circle	54	43.0	104.6	163.3	30.7
2121	8	1	Square	24	58.0	119.1	174.3	
2121	9	1	Square	24	63.4	114.0	174.3	
2121	10	2	Square	38	17.2	70.5	135.0	
2121	11	2	Square	38	14.9	75.1	132.3	17.0
2121	12	1	Circle	37	13.6	76.4	135.0	
2121	13	2	Circle	48	20.6	90.0	155.8	13.8
2183	14	1	Square	48	17.5	78.1	139.4	
2183	15	1	Square	54	23.2	81.5	146.3	
2183	16	2	Square	34	18.4	81.3	137.7	1.9
2183	14	1	Hexagon	59	40.4	108.4	180.0	
2183	16	2	Hexagon	33	48.0	104.0	167.0	3.3
2183	14	1	Circle	47	70.6	116.6	167.5	
2183	17	1	Circle	40	60.3	-	-	
2183	18	2	Circle	31	61.4	122.0	175.2	-3.0